Astron. Astrophys. 333, 1034–1042 (1998)

ASTRONOMY AND ASTROPHYSICS

Intermediate drift bursts and the coronal magnetic field

Arnold O. Benz[1] **and Gottfried Mann**[2]

[1] Institute of Astronomy, ETH-Zentrum, CH-8092 Zürich, Switzerland
[2] Astrophysikalisches Institut, Observatorium für solare Radioastronomie, D-14473 Potsdam, Germany

Received 8 December 1997 / Accepted 27 January 1998

Abstract. We have analyzed 12 decimetric continuum (type IV) events during solar flares showing intermediate drift (IMD) fine structures in the 1 - 3 GHz band. This is the first time IMD patterns have been reported above 1 GHz and that the full spectrum of both continuum and IMD bursts has been covered. The IMD pattern was usually shifted to higher frequency and tends to occur later than the continuum. Average drift rates of IMD bursts per event were found by cross-correlation yielding $\dot{\nu}/\nu$ = -0.167 to -0.046 s^{-1}. The average second derivative of individual IMD bursts expressed as $\ddot{\nu}\dot{\nu}^{-2}\nu$ is 0.42 to 4.19. Normalized by the mean frequency, these high-frequency IMD bursts are found to be identical in their characteristics with this type of bursts below 1 GHz. The derived burst parameters require an important change in one of the two existing theories.

Key words: Sun: corona – Sun: magnetic fields – Sun: flares – Sun: radio radiation

1. Introduction

Intermediate drift (IMD) bursts have been thought to be a most promising way to measure the coronal magnetic field in the 1970's and 1980's (e.g. Tarnstrom & Benz 1978; Mann, Karlický & Motschmann 1987). Have IMD bursts come up to these expectations? IMD bursts have been first detected by Young et al. (1961), who classified them as a separate type of decimetric flare emission. The drift rate of individual IMD structures is roughly one order of magnitude larger than in shock-produced type II bursts at the same frequency and one order of magnitude smaller than the type III bursts emitted by beams of fast electrons. Groups of IMD bursts have also been noticed by Thompson & Maxwell (1962, Fig. 6b) and Slottje (1972), and they appeared in the collections of Bernold (1980) and Slottje (1981), who called them 'fiber bursts'. We will use here the name IMD bursts, given by the first discoverers. More observations were reported by Elgarøy (1982), Bernold & Treumann (1983), Aurass et al. (1987), Chernov (1990) and others. All of these observations were made at frequencies below 1000 MHz. The lowest frequency IMD bursts were reported at 150 MHz (Elgarøy 1982).

Send offprint requests to: A.O. Benz

Already in the 1970's it became clear that IMD bursts are a part of the phenomena called decimetric type IV bursts. The major part of type IV bursts is a continuum emission generally attributed to a coherent emission by trapped, non-thermal electrons (Kuijpers 1974; Stepanov 1974). It is often modulated in time and accompanied by fine structures such as IMD bursts. The IMD pattern tend to occur in the late phase of the type IV bursts (Tarnstrom & Benz 1978). IMD bursts cluster in groups of 10 to 30 individuals each having a total bandwidth of the order of half the center frequency.

The main characteristics of single bursts are: (i) The drift/frequency ratio, $|\dot{\nu}/\nu|$, is of the order of 0.04–0.1 s^{-1}. (ii) The drift rate $\dot{\nu}$ is usually negative, indicating motion towards the low-frequency emitting part of the source. (iii) The duration at a given frequency is one second or less. (iv) The instantaneous bandwidth, $\Delta\nu/\nu$, is about 2% , and (v) a characteristic absorption feature precedes the emission and drifts in parallel.

The optimism expressed in the first sentence of the introduction was based on the interpretation of the IMD phenomena by whistler waves (Kuijpers 1975). The parametric interaction of a Langmuir wave and a whistler was proposed, producing a transverse wave ($L + w \rightarrow t$) that can escape from the emitting plasma. The modulation of the emission into IMD bursts was interpreted by a whistler wave packet propagating through a region of enhanced Langmuir waves.

In the mean time this model has suffered criticism from several sides: (i) Melrose (1975) has pointed out that the parametric conditions of $L + w \rightarrow t$ are difficult to be met by beam-driven Langmuir waves, making this process very inefficient. (ii) Using nonlinear wave packets (solitons), Bernold & Treumann(1983) have demonstrated that a nonlinear $L+w \rightarrow t$ process operates, but the emission of a single soliton is far too weak since whistler solitons have a small volume. Instead, they proposed the nonlinear process as the emission mechanism involving a large number of whistler solitons, but another process for the modulation producing IMD bursts is required. As a possible candidate, they proposed Alfvén solitons changing the emission properties of the whistler solitons in a large volume and thus producing the observed drifting absorption and emission. Thus the drift rate would not be the whistler group velocity as assumed by Kuijpers (1975), but the velocity of the Alfvén soliton.

Güdel et al. (1988) and Treumann et al. (1990) have investigated stationary solutions for Alfvén solitons propagating obliquely to the magnetic field in a two component (hot and cold) corona. They apply a super-Alfvénic solution to modulate the emission and relate the observed range of drifts to velocities between 1 and 3 times the local Alfvén velocity.

Another line has been followed by Mann, Karlický & Motschmann (1987), who proposed a different modification of the original model. They consider low-frequency, form-stable whistler wave packets for both emission and modulation of IMD bursts. The proposed wave packets do not satisfy the conditions for solitons, but are much larger. The ponderomotive force induces a density hump causing the observed absorption feature at the low-frequency side of IMD bursts. The wave packets originate at the bottom of magnetic loops that trap energetic electrons and near the level where the whistler frequency equals the lower-hybrid frequency. The wave packets then propagate upward with the local whistler group velocity.

Thus we are faced with two models of the IMD phenomenon interpreting the drift rate by a few times the Alfvén velocity and the whistler group velocity, respectively. The magnetic field derived from the observations differs by an order of magnitude for the two models. If the interpretation of IMD bursts were settled in either way, the magnetic field in the source could be determined with accuracy.

Here we present the first observations of IMD bursts above 1 GHz. As the data is recorded digitally, the burst parameters can be determined with great precision. Not only the drift rate, $\dot{\nu}$, is measured, but also its derivative in time, $\ddot{\nu}$. The results are compared to the predictions by the Alfvénic soliton and whistler wave packet models in Sect. 3.

2. Observations

New observations of IMD bursts have been made with the very broadband Phoenix spectrometer of ETH Zurich in the 0.1 to 3 GHz range. Details on the instrumentation have been published by Benz et al. (1991). Here we report on the analysis of twelve events that have occurred in the years 1989 to 1993. Their date, time, and frequency of peak IMD activity are listed in Table 1. Since the flare trigger and the channel density were chosen to favor the 1–3 GHz region, all observed IMD bursts occurred above 1 GHz, reaching a maximum frequency of 2.6 GHz (Fig. 2). The frequency-agile spectrometer measured most of the time at 200 channels with a resolution of 10 MHz in frequency and 0.1 s in time. Flux density and circular polarization (Stokes I and V) were recorded. The data has been calibrated and analyed using the standard routines at ETH Zurich (Csillaghy 1997).

2.1. The location of IMD bursts in the spectrogram

The broad bandwidth and the new, high-frequency range of the Phoenix spectrometer allowed for the first time to relate the IMD bursts to the associated type IV continuum event in the spectrogram. A typical example is shown in Fig. 1. In the top part, the total flux density is displayed on a logarithmic scale. The main part of the type IV event is an intense continuum centered at about 1100 MHz. A much weaker continuum extends up to 3000 MHz. It contains weak IMD structure in time and frequency. The IMD bursts in the high-frequency continuum have been enhanced by subtracting a gliding average of 200 MHz bandwidth in frequency and of 5 seconds in time(Fig. 1, bottom).

The time and frequency of maximum IMD activity in each event is given in Table 1. We have also compared the position in frequency and time of the IMD pattern to the maximum of the continuum. The most significant new result is on the location of IMD burst in the spectrum. There is a significant trend for IMD patterns to occur at higher frequency than the spectral peak of the type IV continuum (positive shift). The maximum displacement was 610 MHz. Only in one of the 12 events the IMD bursts were found at clearly lower frequencies. It is presented in Fig. 2. This case is also the event with the highest frequency IMD bursts, reaching up to 2550 MHz. Furthermore, we confirm earlier reports that the IMD bursts tend to occur after the peak of the type IV bursts by up to 26 s; only two out of twelve IMD groups were before.

In 3 of the 12 events, BATSE/GRO has reported an associated hard X-ray flare. In all cases both continuum and IMD bursts have occurred during the decay phase of the hard X-ray flare.

2.2. Properties of individual IMD bursts

The recording of a broadband spectrogram makes it possible to thoroughly investigate the drift of IMD bursts, $\dot{\nu}$, and the second derivative, $\ddot{\nu}$. For this purpose, we selected the most suitable time intervals and parts of the spectrum, and subtracted a gliding background both in time and frequency with a scale exceeding the instantaneous duration and bandwidth of the structures. We then investigated individual IMD bursts and determined the drift rate and mean frequency by measuring the time and frequency of the maximum near the start and end of all well-defined single bursts. The result for eight events with the largest number of single bursts and sufficient for a statistical study is shown in Fig. 3.

The drift rate of individual IMD bursts normalized by the mean frequency scatters by up to a factor of two within the same event. IMD groups with different characteristics are presented in the examples of Figs. 1 and 2. Fig. 1 contains IMD bursts with drift rates between $\dot{\nu}/\nu = -0.160$ s^{-1} and -0.090 s^{-1}. The second derivative changes even more, from $\ddot{\nu}/\nu = 7.8 \cdot 10^{-4}$ s^{-2} at high frequencies to $3.2 \cdot 10^{-2}$ s^{-2} at low frequencies. The event of Fig. 2 shows much less scatter. The first derivative varies only within 10% around the value from cross-correlation, $\dot{\nu}/\nu = -0.046$ s^{-1} at $\nu = 2.29$ GHz. The second derivative, correspondingly, scatters only 20% around $\ddot{\nu}/\nu = 3.5 \cdot 10^{-3}$ s^{-2}. The two events are extreme in the disparity of the ranges in which the parameters of individual IMD bursts vary.

The smallest drift rates of all individual IMD bursts was $\dot{\nu}/\nu$ = -0.0406 s^{-1}, and the maximum value was found at -0.230 s^{-1}.

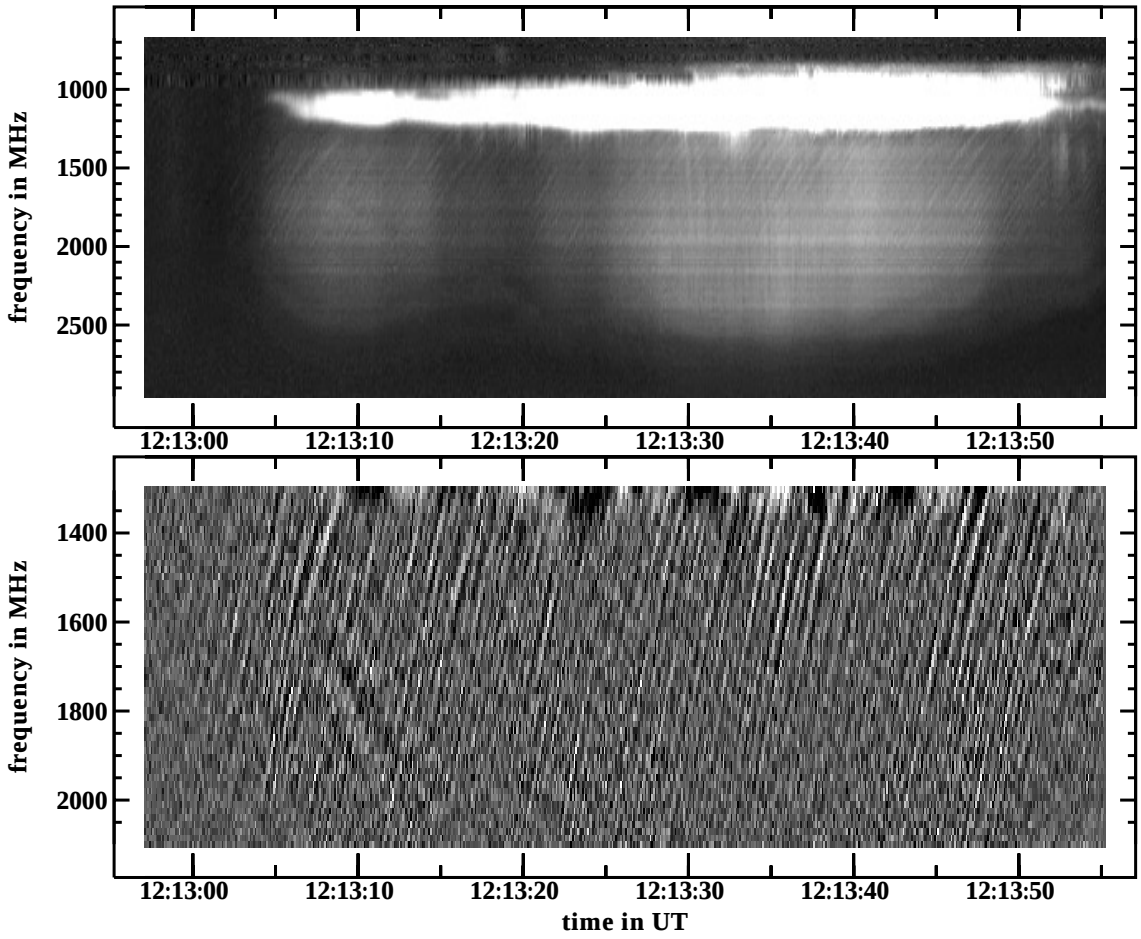

Fig. 1. *Top:* Spectrogram of a decimetric type IV burst observed with the Phoenix radio spectrometer of ETH Zurich on March 20, 1993. The preburst background has been subtracted, and the greyscale is logarithmic. *Bottom:* The intermediate drift bursts have been enhanced by subtracting a gliding average in frequency and time.

Table 1. List of analyzed events with Intermediate Drift fine structures: mean time and frequency of peak IMD activity, shift to peak continuum activity, and average parameters of bursts

date yymmdd	mean time hhmmss	mean frequ. MHz	shift s	shift MHz	first derivative MHz/s	second derivative MHz/s^2	k ratio
890901	061229	2290	-12	-130	-102.5±8	4.8± 2	1.05
890914	093135	1050	47	400	-88.7± 5	14.6± 3	1.95
900404	132248	1680	20	180	-149.6± 8	29.4± 3	2.21
900415	081216	1200	–	–	-43.7±2	6.7± 2	4.19
900615	083013	1075	21	275	-100.5±10	37.0± 3	3.94
900730	080910	1085	-2	230	-65.2±3	8.1 ± 3	2.07
910718	143200	1650	6	0	-88.3±2	2.0± 0.6	0.42
930107	090140	1350	5	600	-64.9±3	6.3± 2	2.02
930320	120446	1195	-14	0	-101.5±20	11.0± 5	1.28
930320	121340	1740	7	610	-196.2±10	18.7± 8	0.85
930320	144005	1260	6	160	-159.4± 8	19.1± 3	0.95
930320	150434	1321	15	300	-244.0±20	37.5± 10	0.83

2.3. Average properties of IMD groups

For the the average properties of IMD groups we used the cross-correlation of the most prominent channel in IMD burst activity (mean frequency given in Table 1) with all the other relevant channels. The cross-correlation yields reliable average characteristics if the bursts are not too different in drift rate or peak flux. Fig. 4 is an example, showing a pronounced structure through the center with a peak of 1.0 at zero delay and at 1740 MHz (auto-correlation channel).

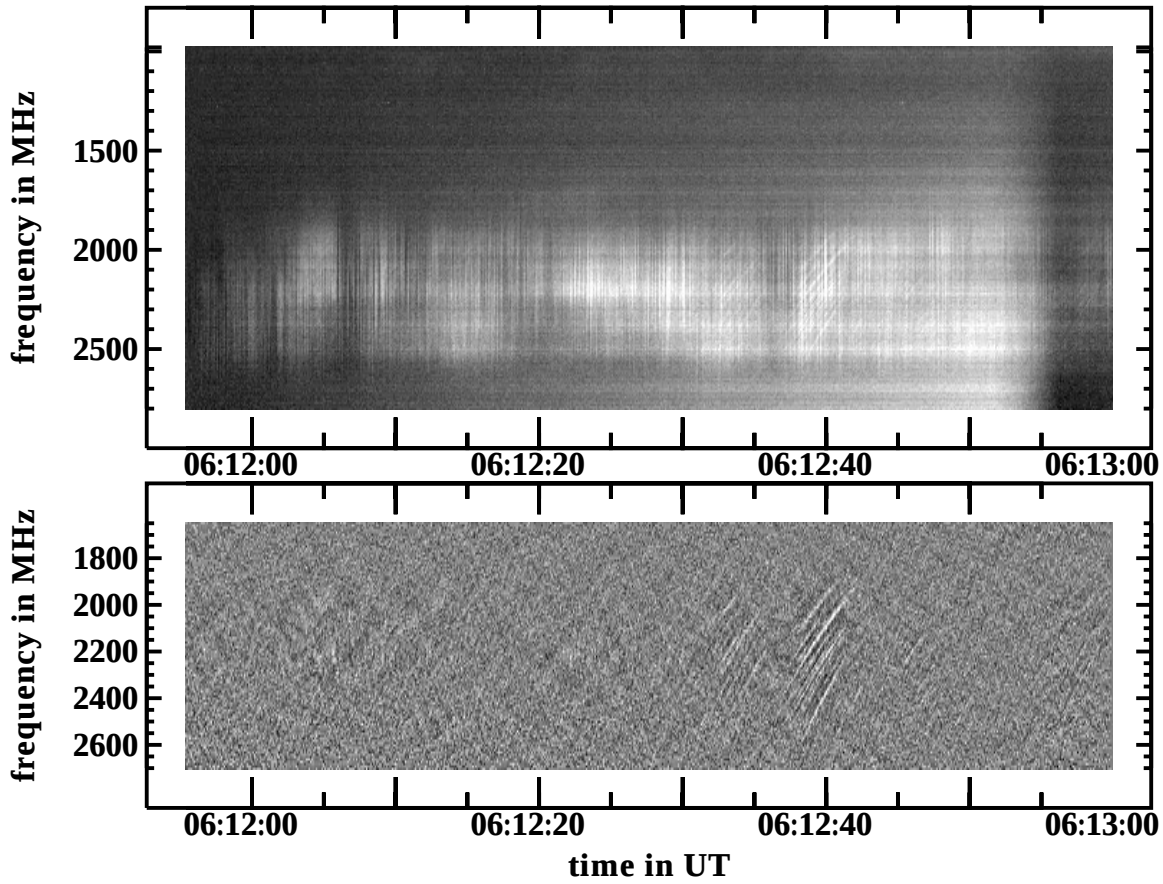

Fig. 2. *Top:* Spectrogram of a decimetric type IV burst observed with the Phoenix radio spectrometer of ETH Zurich on September 1, 1989. The preburst background has been subtracted, and the greyscale is logarithmic. *Bottom:* The intermediate drift bursts have been enhanced by subtracting a gliding average in frequency and time.

The average drift rate (first derivative of peak frequency in time) was found from the cross-correlogram in the frequency-time plane (e.g. Fig. 4). The peak values were plotted in ν vs. t diagrams (cf. Fig. 5 left as an example) and fitted by various procedures to reduce the noise: spline, second, third and fourth order polynomials, and gaussian fits. The fitted curve was then derived in time to find the drift rate (Fig. 5 middle). It was fitted again to evaluate the second derivative (Fig. 5 right).

The results of the different fitting methods can be seen in the example of Fig. 5 right. In general, they differ only slightly in the first derivative, but considerably in the second derivative. The largest deviations are at both ends of the frequency range. At the mean frequency, for Fig. 5 right in the middle of the displayed range at 1740 MHz, the values usually converge well. Their range at the mean frequency was taken as indication of the accuracy, which is listed in Table 1. Also listed are the values of the drift rate and the second derivative at the mean frequency using third-order fits.

Note that the *average* drift rate in different events scatters even more than individual IMD structures of the same event. The average $\dot{\nu}/\nu$ values differ by more than a factor 3, ranging from $\dot{\nu}/\nu$ = -0.167 to -0.046 s^{-1}. In particular, the IMD bursts of the 93/03/20 events (Fig. 3) drift significantly faster than most others.

Fig. 6 displays graphically the average drift rates listed in Table 1. Indicated by crosses are the mean values at lower frequencies derived by Bernold (1983). They have been extrapolated by a second order (parabolic) fit to higher frequencies, using the following parameters

$$\dot{\nu} = -0.36 - 0.015\nu_{MHz} - 3.7 \cdot 10^{-5}\nu_{MHz}^2 \quad \mathrm{MHz/s}, \qquad (1)$$

where ν_{MHz} is the mean frequency in MHz. Fig. 6 suggests that the extrapolated curve is an acceptable fit also at higher frequencies. However, there is considerable scatter, much larger than the statistical uncertainty.

No significant correlation was found between the average second derivative and the mean frequency as listed in Table 1. However, Fig. 7 indicates that the second derivative is related to the drift rate. The data has been complemented by low-frequency values derived from the mean drift rates given by Bernold (1983). If those values are again extrapolated by a second-order fit to higher frequencies (dashed), the observed values seem to be well represented. However, the apparent fit is somewhat feigned by the event at -100.5 MHz/s and 37.0 MHz/s^2 (event 90/06/15 0830) with only 3 IMD bursts, by far the smallest number of all events. The linear regression (first-order

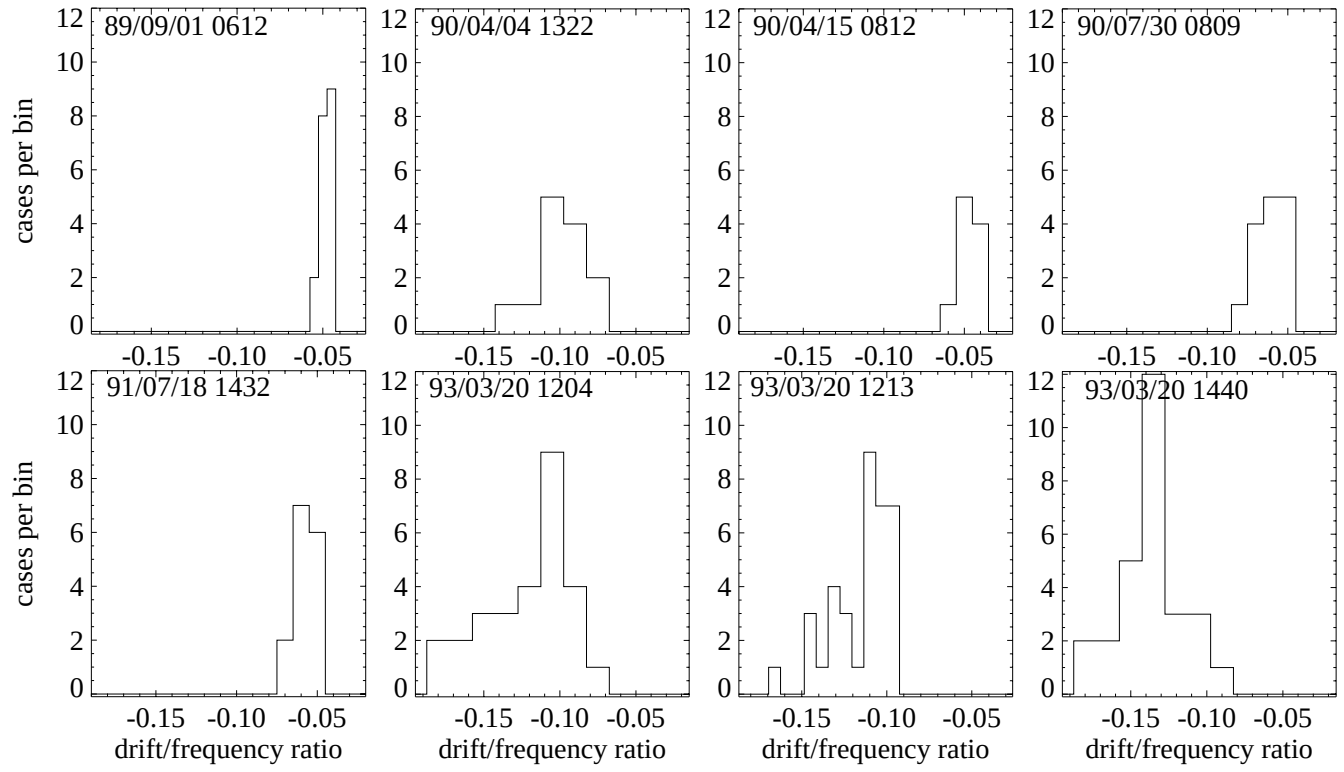

Fig. 3. The distribution in drift rate of single IMD bursts measured in the eight events with the largest number of bursts. The drift rate has been normalized by the mean frequency between start and end points. The ordinate is $\dot{\nu}/\nu$ in units of s^{-1}.

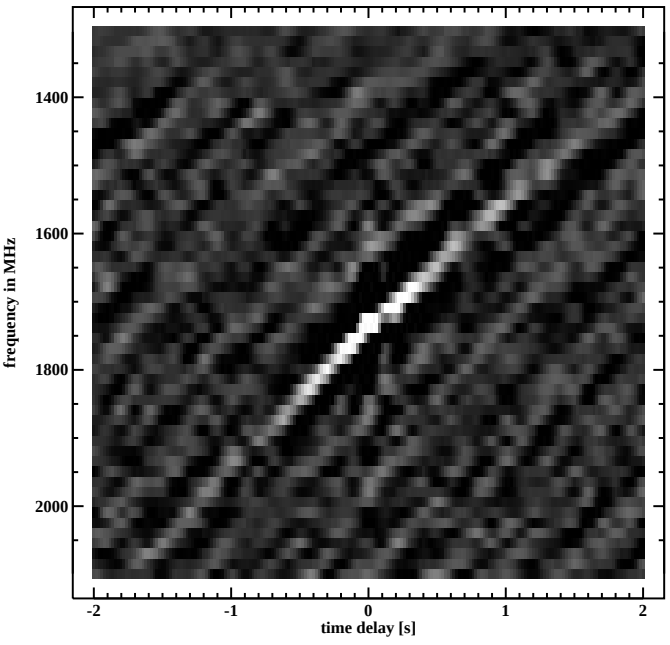

Fig. 4. Cross-correlogram of IMD bursts in time. The data of Fig. 1 (bottom, gliding average) has been cross-correlated with the frequency channel 1740 MHz. The correlation coefficients are shown in a linear greyscale and in pseudo-spectrogram representation.

fit) is a better representation of the average second derivative. It is given by

$$\ddot{\nu} = -0.517 - 0.143\dot{\nu}_{MHz} \quad \mathrm{MHz/s^2}, \tag{2}$$

where $\dot{\nu}_{MHz}$ is the drift rate in MHz/s.

It is important to note that the second term, proportional to $\dot{\nu}$, dominates Eq. (2). It suggests that the drift rate of individual IMD bursts is related to the instantaneous emission frequency such that in the average $\dot{\nu} \sim \nu$. This result is also manifest in Fig. 5 middle, where $\dot{\nu}/\nu = 0.110 \pm 0.003$ s^{-1} over the range from 1450 to 2005 MHz. The dependence of the drift rate on frequency therefore is different whether the average behavior in one event is considered (Fig. 5) or the mean values of different events are compared (Fig. 6).

Finally the ratio k is given in Table 1. It is defined by

$$k = \frac{\nu\ddot{\nu}}{(\dot{\nu})^2} \quad . \tag{3}$$

The measured ratio has a range of 0.42 to 4.19 at the mean frequency of IMD activity. The values given in Table 1 and gaussian error propagation yield an average accuracy in k of 39% with individual values reaching up to 80%. The mean k value is 1.81, and the median is 1.62. The linear regression above 1 GHz and the values below derived from Bernold (1983) suggest an *average* k value of 1.3±0.2.

3. Theory and discussion

In this discussion it is assumed that IMD bursts appearing in the whole range from 100 MHz to 3 GHz are generated by

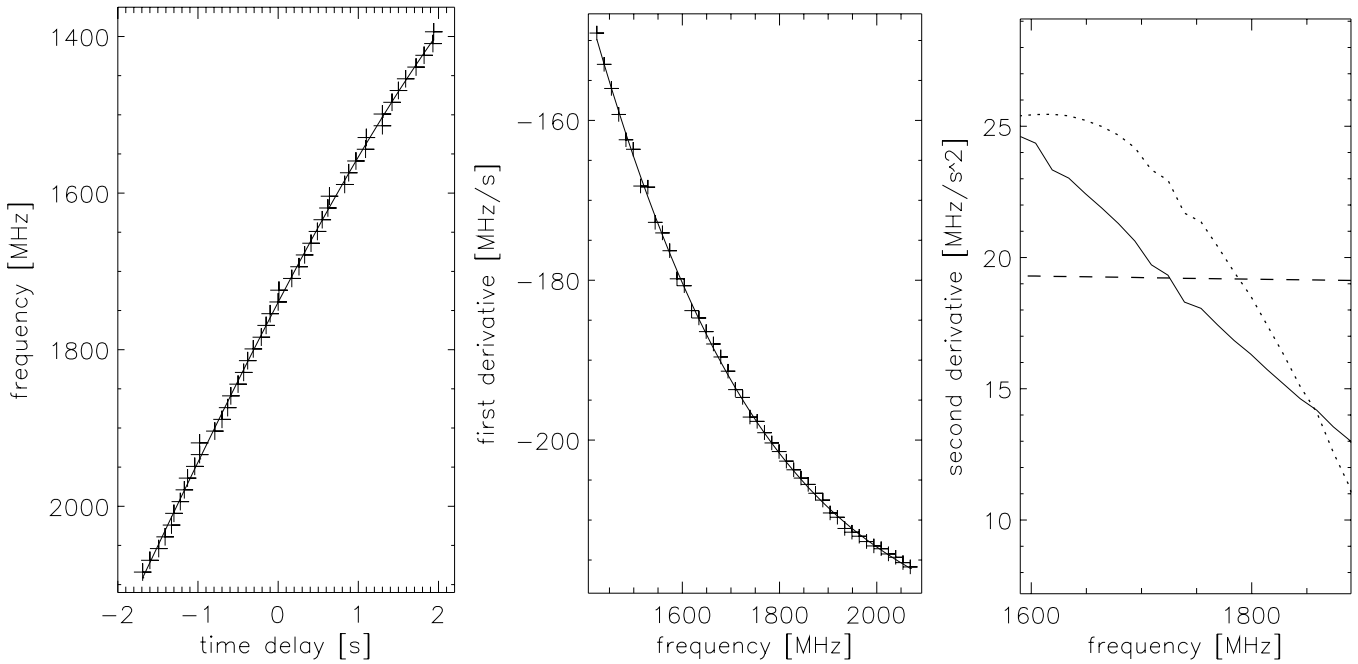

Fig. 5. *Left:* The peak of the cross-correlation shown in Fig. 4 was marked in each channel and fitted with a third-order polynomial (thin curve). The curve represents the average IMD characteristics of the 93/03/20 1213 UT event. *Middle:* The drift rate (first derivative) of the fitted curve in the left image was derived vs. time and is shown by crosses. This was again fitted by a third-order polynomial (thin curve). *Right:* The second derivative, using the fitted first derivative is shown (full curve). Also presented are the results of other fits: dotted for a fourth-order polynomial and dashed for a gaussian fit.

the same mechanism. According to Eq. (1) typical drift rates $\dot{\nu}$ of -180 MHz/s and -5 MHz/s are found at 2000 MHz and 200 MHz, respectively. The drift rate $\dot{\nu}$ at the frequency ν is related to the modulator velocity V producing the IMD structure by

$$V = -\frac{\dot{\nu}}{\nu} \cdot H \tag{4}$$

with the scale of height H depending on the type of emission: For plasma emission, the observed frequency is approximately the plasma frequency in the source

$$\nu_p^e = \sqrt{\frac{e^2 n_e}{\pi m_e}} \ , \tag{5}$$

or its harmonic (e = elementary charge, n_e = electron number density, m_e = electron mass). For plasma emission the scale height corresponds to twice the density scale height, thus $H = 2H_n/\cos\theta$. If the propagation angle θ of the modulator relative to the vertical is close to zero and the coronal temperature 2×10^6 K, H $\approx 2 \times 10^5$ km. Then, the drift rates correspond to source velocities of 18000 km/s and 5000 km/s at the 2000 MHz and 200 MHz plasma level, respectively. For gyroemission at a harmonic of the electron gyrofrequency, the scale height of the magnetic field, H_B, must be used. It is not well known, probably very variable and expected to be usually less than H_n. Thus gyroemission generally predicts smaller modulator velocities.

Additionally, two requirements, which are independent from the models, should be taken into account:

– The sources of IMD bursts are likely to be located within stable coronal loops. This requires $\beta \lesssim 0.5$, where $\beta = 8\pi n_e k_B T/B^2$ (k_B = Boltzmann's constant).
– The solar corona generally satisfies $\omega_p^e/\Omega_e > 1$. This condition is a requirement for plasma emission.

These conditions provide approximate upper and lower limits on the magnetic field in the source region. Thus, the magnetic field B should be in the ranges
26 G < B < 715 G at ν_p^e = 2000 MHz
2.6 G < B < 72 G at ν_p^e = 200 MHz .

3.1. Alfvén wave model with plasma emission

As mentioned in Sect. 1, two models have been proposed for IMD bursts. One model considers the IMD bursts as plasma emission modulated by Alfvén solitons traveling upwards in a coronal loop (Treumann et al. 1990). In this case the source velocity is between 1 and 3 times the local Alfvén speed v_A, defined by

$$v_A = \frac{B}{\sqrt{4\pi \bar{m} n_i}} \ , \tag{6}$$

with B and n_i as the local magnetic field strength and the ion number density, respectively. The mean ion mass, $\bar{m}$, is taken as $1.26 m_p$, the proton mass. Assuming that the source velocity V of IMD bursts is twice the Alfvén velocity v_A and that the radiation frequency is proportional to the plasma frequency, a magnetic field strength of 920 G and 26 G is deduced from

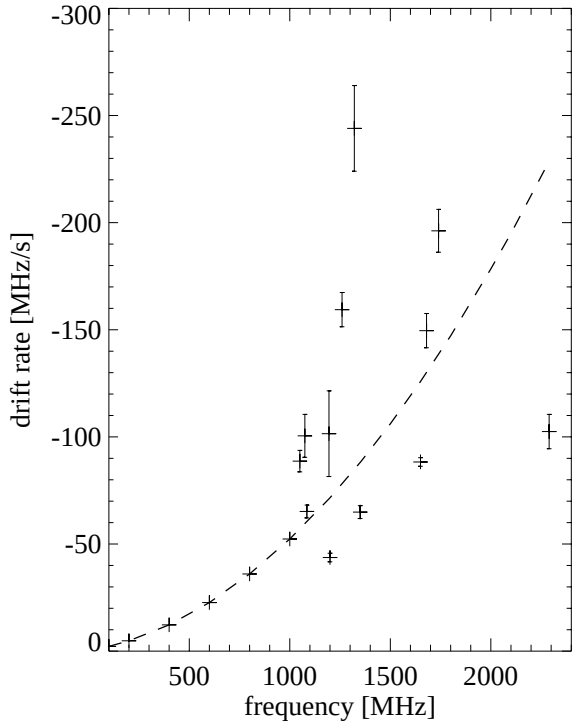

Fig. 6. The average drift rate of the 12 IMD events vs. frequency is shown with error bars. The average drift rate measured at lower frequency by Bernold (1983, simple crosses) has been fitted by a second order polynomial (dashed curve) and extrapolated to higher frequency for comparison.

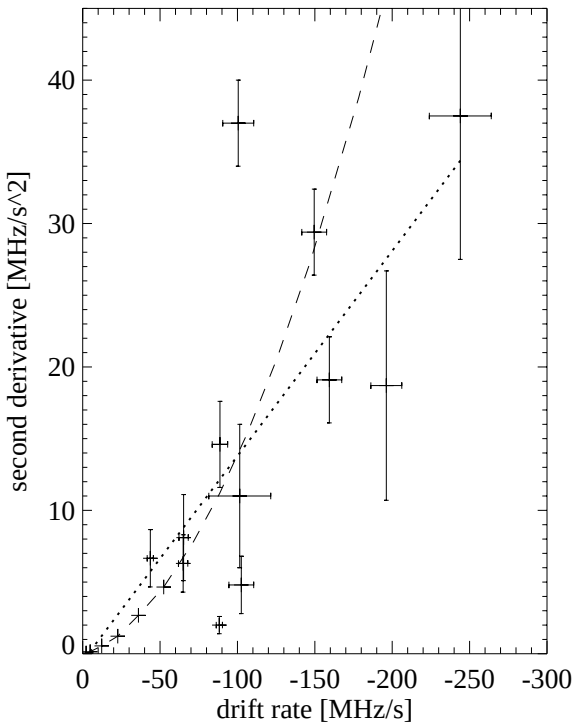

Fig. 7. The average drift rates are compared to the average second derivatives of the 12 IMD events. Low-frequency second derivatives have been computed from the frequency dependence of the average drift rates given by Bernold (1983). The average second derivatives have been fitted by a second order polynomial (dashed curve) and a linear regression (first order polynomial, dotted curve).

Eqs. (5) and (6) at the 2000 MHz and 200 MHz frequency level, respectively. In the most extreme case of Table 1, the magnetic field would correspond to a ratio $\omega_p^e/\Omega_e = 0.34$ in the source volume. This is contrary to the above requirement for plasma emission.

3.2. Alfvén wave model with electron cyclotron maser emission

As an alternative, a new model is proposed here, in which the radio emission is produced by maser emission at a harmonic of the electron cyclotron frequency and the IMD modulation by an Alfvénic soliton. The maser process operates for energetic electrons trapped in a coronal loop and thus having a loss-cone distribution in velocity space. It is significant if $\omega_p^e/\Omega_e \lesssim 1$ (Wu & Lee 1979; Melrose et al. 1984; Sharma & Vlahos 1984). This condition is hardly met in the regular corona. However, if a significant population of hot particles increases, the pressure in a loop-shaped flux tube cannot be counterbalanced at both ends. The overpressure will eventually reduce the particle density in the flux tube and ω_p^e/Ω_e diminishes. Such evacuated flux tubes are amenable to electron maser emission.

The above scenario is supported by the observations that decimetric type IV bursts generally occur after the impulsive phase of flares. Furthermore, the IMD pattern is usually found in the later phase of type IV events (cf. Sect. 1).

The maser model proposes that the trapped electrons drive waves at a low harmonic of the electron gyrofrequency. The waves are electromagnetic and escape directly as radio emission if $\omega_p^e \lesssim 0.3\Omega_e$. They are electrostatic (if $0.3\Omega_e \lesssim \omega_p^e \lesssim \Omega_e$) and are transformed into electromagnetic radio waves by coalescence. In both cases

$$\omega_t = s\,\Omega_e \quad . \tag{7}$$

The drift rate is analogous to Eq. (4)

$$\dot{\nu} \approx -\frac{\nu\alpha v_A}{H_B} \quad , \tag{8}$$

where α is between 1 and 3. The most likely value, $\alpha = 2$, will be used in numerical estimates. The Alfvén velocity refers to the local value at the emission site and is given by Eq. (6). Using Eq. (7),

$$\dot{\nu} \approx -\frac{\alpha c}{sH_B}\left(\frac{m_e n_e}{\bar{m} n_i}\right)^{1/2}\frac{\nu^2}{\nu_p^e} \quad , \tag{9}$$

If $\alpha/sH_B\nu_p^e$ is roughly constant, Eq. (9) predicts an approximately parabolic dependence on ν. This is confirmed by observations (Fig. 6) and Eq. (1).

According to Eq. (9), the second derivative is

$$\ddot{\nu} = \frac{2\dot{\nu}^2}{\nu}\left(1 - \frac{H_B\cos\theta}{4H_n}\right) \approx \left(\frac{4sH_B}{\alpha c\cos\theta}\right)^{1/2} \mid \dot{\nu} \mid^{3/2} \quad . \tag{10}$$

The power-law dependence on $\dot{\nu}$ is consistent with observations (Fig. 7). Eq. (10) yields

$$k = 2\left(1 - \frac{H_B \cos\theta}{4H_n}\right) \quad . \tag{11}$$

Observations suggest that $H_B \leq H_n$ (e.g. Dulk & McLean 1978). Eq. (11) then yields a range of k-values between 1.5 and 2, much narrower than observed. Although variable H_B and θ may enhance the scatter in k, this poses a serious problem to the maser emission model.

The magnetic fields derived at the 2000 MHz and 200 MHz levels, using Eq. (7) and $s = 5$, are 143 G and 14 G, respectively. This result is compatible with the above requirements.

3.3. Whistler wave model

In the other model, the IMD bursts are generated by packets of low frequency whistler waves propagating along the magnetic field lines of a coronal loop. The drift of IMD bursts then relates to the whistler group velocity v_g given by

$$v_g = 2c \cdot \frac{\Omega_e}{\omega_p^e} \cdot \sqrt{x(1-x)^3} \tag{12}$$

with $x = \omega_w/\Omega_e$. It is important to note here that ω_w denotes the whistler frequency, fixed at the source of the wave packet. Theoretical investigations (e.g. Berney & Benz 1978, Mann et al. 1989) suggest that the most unstable waves are at $\omega_w \approx 0.03 \cdot \Omega_e$ in the source. Thus initially $x \approx 0.03$, and x decreases from this value with propagation into weaker magnetic fields. The parethesis in the square root of Eq. (12) will thus be neglected. According to the model the radio waves are generated by coalescence of whistler waves and upper hybrid waves into escaping electromagnetic waves (Kuijpers 1975). Both wave modes are excited by an energetic electron population trapped in a coronal loop and, consequently, developing a loss-cone distribution. For $\omega_p^2 > \Omega_e^2$ the emission is at the upper hybrid frequency. Thus

$$\omega_t = \sqrt{\omega_p^2 + \Omega_e^2} \approx \omega_p \quad . \tag{13}$$

Eqs. (4) and (5) then become

$$\dot{\nu} = -\frac{c\cos\theta\sqrt{\Omega_e \omega_w}}{2\pi H_n} \quad . \tag{14}$$

Although Eq. (14) does not contain ν explicitely, $\dot{\nu}$ depends on ν through Ω_e. If Ω_e/ω_p is roughly constant along the path of whistler propagation, $\dot{\nu} \sim \sqrt{\nu}$. The observations (cf. Fig. 6) and Eq. (1) require a stronger dependence. A possible way out is a declining θ caused by the loop bending over.

For constant H_n, θ, and H_B, one derives from Eq. (14)

$$\ddot{\nu} = \frac{c^2 \omega_w \cos\theta}{2\pi H_n H_B} \frac{\Omega_e}{\omega_t} \quad . \tag{15}$$

Thus,

$$k = \frac{H_n}{H_B \cos\theta} \quad . \tag{16}$$

Again, the ν-dependence of $\ddot{\nu}$ does not agree with the observations. However, the range of k-values is larger since $k \geq 1$, and is more in agreement than the Alfvén wave model.

The magnetic field can be derived from Eq. (14)

$$B = \frac{2\pi|\dot{\nu}|m_e}{e\sqrt{x}\cos\theta} \quad . \tag{17}$$

Using the fitted value of $\dot{\nu}$ in Eq. (1), $\theta \approx 0$ and $x = 0.01$, the field strengths at 2000 MHz and 200 MHz are 212 G and 5.7 G, respectively.

4. Conclusions

New observations allow to investigate IMD structures up to 2550 MHz and to analyze them with greatly enhanced precision. These broadband observations show them generally located in the high-frequency part of the type IV continuum and in its later phase.

The quantitative results on the first derivative (drift rate) and second derivative have been used to test the two existing models. At the newly accessible high frequencies, the Alfvén soliton model by Treumann et al. (1990) predicts very high magnetic fields that are inconsistent with plasma emission. The model may be modified by proposing electron maser emission in evacuated flux tubes. The k-values are then derived to be in a small range between 1.5 and 2.0, contrary to the observed range of 0.42 to 4.19.

The other model, suggesting whistler waves (e.g. Mann et al. 1987), predicts relations of $\dot{\nu}$ and $\ddot{\nu}$ with frequency dependances that contradict the observations.

The discrepancies may be resolved for both models by allowing more parameteres to vary systematically with height, for instance θ and H_B. This investigation then exhibits a general problem facing complex models with many free parameters: They can often be adapted to fit the observations. Thus it is not possible to decide definitively between the models.

As an example, the following parameters are derived from the observations at 2 GHz: The whistler model yields an electron density of $5 \times 10^{10}\mathrm{cm}^{-3}$ and a magnetic field of 212 G; the soliton model yields $4.2 \times 10^{29}/H_B^2\mathrm{cm}^{-3}$ and 143 G.

The adaption of the Alfvén soliton model to maser emission has the effect to diminish the discrepancies in the determination of the magnetic field strength between the two models. They differ by less than a factor of 2.5 in the range from 200 to 2000 MHz (10 G to 200 G), and in the restricted range of 1 - 2 GHz, relevant for these observations, the difference is less than a factor of 1.5. It may make IMD bursts attractive to measure magnetic fields in post-flare loops in spite of the uncertain physics.

Acknowledgements. The operation of the Phoenix spectrometer is a team effort. We would like to thank in particular A. Csillaghy for developing calibration and analysis software, and M.J. Aschwanden for help with BATSE data. Hardware construction and some of the data analysis are financed by the Swiss National Science Foundation grant 20-46656.96.

References

Aurass H., Chernov G.P., Karlický M., Kurths J., and Mann G., 1987, Solar Phys. 112, 347
Berney, M. and Benz, A.O., 1978, Astron. Astrophys. 65, 369
Bernold T.X.B., 1980, A&AS 42, 43
Bernold T.E.X., 1983, Thesis, ETH Zurich
Bernold T.E.X. and Treumann R.A., 1983, ApJ 264, 677
Benz A.O., Güdel M., Isliker H., Miszkowicz S., and Stehling W., 1991, Solar Phys. 133, 385
Chernov G.P., 1990, Sov.Astron. 34, 66
Csillaghy A., 1997, Dissertation nr. 12239, ETH Zurich
Dulk G.A., and McLean D.J., 1978, Solar Phys. 57, 279
Elgarøy Ø., 1982, Rep.No. 53, Inst. Theoret. Astrophys. Bildern-Oslo
Güdel M., Benz A.O., and Treumann R.A., 1988, *Proceedings of the Joint Varenna-Abastumani Workshop on Plasma Astrophysics*, ESA SP-285 1, 95
Hada, T., Kennel, C. F., and Teresawa, T., 1987, J. Geophys. Res. 92, 4423
Krall, N. A. and Trivelpiece, A. W., 1973, *Principles of Plasma Physics*, McGraw-Hill, New York
Kuijpers J., 1974, Solar Phys. 36, 157
Kuijpers J., 1975, Solar Phys. 44, 173
Mann G., Karlický M., and Motschmann U., 1987, Solar Phys. 110, 381
Mann G., Baumgaertel K., Chernov G. P., and Karlicky M., 1989, Solar Phys. 120, 383
Melrose D.B., 1975, Aust.J.Phys. 28, 101
Melrose D.B., Hewitt R.G., Dulk G.A., 1984, JGR 89, 897
Sharma R.R., Vlahos L., 1984, ApJ 280, 405
Slottje C., 1972, Solar Phys. 25, 210
Slottje C., 1981, *Atlas of Fine Structures of Dynamic Spectra*, Dwingeloo, The Netherlands
Stepanov A.V., 1974, Soviet Astron. 17, 781
Thompson A.R. and Maxwell A., 1962, ApJ 136, 546
Treumann R.A., Güdel M., and Benz A.O., 1990, A&A 236, 242
Wu C.S., Lee L.C., 1979, ApJ 230, 621
Young C.W., Spencer C.L., Moreton G.E., and Roberts J.A., 1961, ApJ 133, 243